SnO 2 nanocrystals synthesized by microwave-assisted hydrothermal method: Towards a relationship between structural and optical properties

ARTICLE *in* JOURNAL OF NANOPARTICLE RESEARCH · FEBRUARY 2012

Impact Factor: 2.18 · DOI: 10.1007/s11051-012-0750-7

11 AUTHORS, INCLUDING:

Mário Lúcio Moreira
Universidade Federal de Pelotas
28 PUBLICATIONS **624** CITATIONS
SEE PROFILE

Sergio Mazurek Tebcherani
State University of Ponta Grossa
50 PUBLICATIONS **264** CITATIONS
SEE PROFILE

Jose A. Varela
São Paulo State University
838 PUBLICATIONS **12,810** CITATIONS
SEE PROFILE

Elson Longo
São Paulo State University
875 PUBLICATIONS **14,765** CITATIONS
SEE PROFILE

J Nanopart Res (2012) 14:750
DOI 10.1007/s11051-012-0750-7

RESEARCH PAPER

SnO_2 nanocrystals synthesized by microwave-assisted hydrothermal method: towards a relationship between structural and optical properties

Paulo G. Mendes · Mario L. Moreira · Sergio M. Tebcherani · Marcelo O. Orlandi · J. Andrés · Maximu S. Li · Nora Diaz-Mora · José A. Varela · Elson Longo

Received: 30 November 2010 / Accepted: 17 January 2012 / Published online: 12 February 2012

Abstract The exploration of novel synthetic methodologies that control both size and shape of functional nanostructure opens new avenues for the functional application of nanomaterials. Here, we report a new and versatile approach to synthesize SnO_2 nanocrystals (rutile-type structure) using microwave-assisted hydrothermal method. Broad peaks in the X-ray diffraction spectra indicate the nanosized nature of the samples which were indexed as a pure cassiterite tetragonal phase. Chemically and physically adsorbed water was estimated by TGA data and FT-Raman spectra to account for a new broad peak around 560 cm^{-1} which is related to defective surface modes. In addition, the spherical-like morphology and low dispersed distribution size around 3–5 nm were investigated by HR-TEM and FE-SEM microscopies. Room temperature PL emission presents two broad bands at 438 and 764 nm, indicating the existence of different recombination centers. When the size of the nanospheres decreases, the relative intensity of 513 nm emission increases and the 393 nm one decreases. UV–Visible spectra show substantial changes in the optical absorbance of crystalline SnO_2 nanoparticles while the existence of a small tail points out the presence of localized levels inside the forbidden band gap and supplies the necessary condition for the PL emission.

Keywords SnO_2 · Nanoparticles · Microwave-assisted hydrothermal · Luminescence · Quantum confinement

P. G. Mendes · S. M. Tebcherani
Department of Materials Science, INCTMN, LIMAC, CIPP, UEPG-Universidade Estadual de Ponta Grossa, Av. Gal. Carlos Cavalcanti, 4748, Campus, Uvaranas, Ponta Grossa, PR CEP 84035-900, Brazil

M. L. Moreira (✉) · M. O. Orlandi · J. A. Varela · E. Longo
Department of Physical Chemistry, Institute of Chemistry, INCTMN, LIEC, UNESP-Universidade Estadual Paulista, Prof. Francisco Degni Street, s/no, Quitandinha, Araraquara, SP 14800-900, Brazil
e-mail: mlucio@liec.ufscar.br

J. Andrés
Department of Experimental Sciences, University of Jaume I, 12071 Castellón de la Plana, Spain

M. S. Li
Instituto de Física, INCTMN, USP, P.O. Box 369, São Carlos, SP 13560-970, Brazil

N. Diaz-Mora
Parque Tecnológico de Itaipu (PTI), Laboratório de Materiais (LAMAT/UNIOESTE), Foz do Iguaçu, Brazil

Introduction

The continuing trend toward miniaturization associated with low cost techniques requires preparation methods with refined control on the size and the shape of particles (Mao and Wong 2005). Therefore, it will

be of fundamental and technological interest to develop facile and effective methods to get ready metal oxide nanostructures with fine shape and size control. Tin oxide (SnO_2) is perhaps one of the most intriguing materials to be investigated today, possessing many unique properties for various cutting-edge applications ranging from gas sensing to catalyst and optical electronic devices (Epifani et al. 2006; Pianaro et al. 1995, 1998; Jiang et al. 2005; Batzill 2006; Moreira et al. 2006). SnO_2 is an important n-type metallic oxide semiconductor with a wide band gap (3.6 eV) at room temperature. At the nanoscale level, this materials exhibit fascinating properties that differ drastically from their bulk counterparts (Alivisatos 1996 #47; El-Sayed 2004 #27; Huang et al. 2005#20; Roduner 2006 #13).

It is well known that the size and the morphology of the nanomaterials greatly affect their properties as well their further applications due to their high surface-to-volume ratio, enhanced characteristics of quantum size effects, and high fraction of chemically similar surface sites (Zhu et al. 2006). However, the diameter of SnO_2 nanocrystals is required to be smaller or comparable to its exciton Bohr radius (2.7 nm) for the emergence of the quantum confinement effect and this limits their applications to some extent. If this limitation can be overcome, unique properties such as a blue shift of the band edge transition energy, unusual structural and optical properties can be sensed (Leite et al. 2000).

Bulk SnO_2 is not very luminescent (Her et al. 2006) while nanosized SnO_2 nanoparticles and nanoribbons have been shown to exhibit an intense broad luminescence (400–600 nm) when they are excited by ultraviolet (UV) light (Hu et al. 2003a; Cai et al. 2005; Luo et al. 2006), X-ray (Zhou et al. 2006b), or high-energy electrons. Nanosized SnO_2 structures such as nanobelts (Orlandi et al. 2008), nanotubes (Zhao et al. 2007), and nanodisks (Dai et al. 2002b) has been prepared with moderate success. Some methods, such as hydrothermal (Fang et al. 2009) and solvothermal (Zhu et al. 2006; Liu et al. 2008; Cheng et al. 2004), chemical vapor condensation (Liu et al. 2001b), spark processing (Chang and Park 2002), sputtering and laser ablation (Wang 2003 #32; Gole and Wang 2001#37; Sun et al. 2003 #33; Hu et al. 2003a, b #30) as well as colloidal growth (Ribeiro et al. 2004) assisted by a dialysis process have been employed. Also, the sol–gel (Cao et al. 2006), chemical vapor deposition (Liu et al. 2001b), rapid oxidation of metal tin (Hu et al. 2003a), spray pyrolysis (Paraguay-Delgado et al. 2005), thermal evaporation of oxide powders (Dai et al. 2002a), and molten salt methods have been applied (Liu et al. 2001a). To obtain quantum size SnO_2 nanocrystallites, the sol–gel method (Del Castillo et al. 2005) and hydrolysis of $SnCl_2{\cdot}2H_2O$ have been reported in the literature (Zhu et al. 2006). Recently, SnO_2 quantum dots were also fabricated using hydrazine hydrate as the mineralizer instead of NaOH by a hydrothermal route (Paraguay-Delgado et al. 2005). However, relatively high temperatures and/or elaborated stages during the synthesis are necessary for these methods and further thermal annealing is usually necessary to obtain good crystalline samples (Jouhannaud et al. 2008). Therefore, the development of synthetic routes for the production of SnO_2 nanostructures with controlled size and tunable shapes by wet chemical methods (Jiang et al. 2005; Chen and Gao 2004) remains a challenge.

Recently, several efforts devoted to the synthesis of metal oxide nanostructures with controlled morphologies have produced promising results.(Patzke et al. 2010) Microwave-mediated synthesis for organic molecules and inorganic nanomaterials is of broad interest during the past decade. In particular, an alternative method using a hydrothermal route assisted by microwave radiation heating has emerged in the field of powder preparation with both expected and unexpected merits, e.g., kinetic enhancement, reaction temperature, time reduction, and homogeneous temperature during all annealing processes with controllability over particle sizes (Mao and Wong 2005 #80; Volanti et al. 2008 #84; Rao et al. 1999 #88; Komarneni et al. 1992 #49; Krishna and Komarneni 2009 #95). In 1992, Komarneni et al. (1992) introduced the microwave-assisted hydrothermal (MAH) method for the synthesis of electroceramic powders, a genuine low temperature and fast reacting rate method (Komarneni et al. 1992; Krishna and Komarneni 2009). In particular, these authors have also reported the synthesis of SnO_2 by conventional hydrothermal and MAH methods using different temperatures and additives. In this respect, microwave heating is emerging as a rapid and environmentally friendly mode of heating for the generation of nanomaterials and very recently different reviews have been published where clean, fast, and high yielding reactions under microwave conditions have been emphasized (Baruwati et al. 2009; Bilecka and Niederberger 2010; Strauss and Rooney 2010).

Therefore, microwave irradiation is now recognized as an attractive method for the synthesis of nanocrystals and has the advantages of short reaction time, small particle size, narrow particle size distribution, and high purity.(Raghuveer et al. 2006; Gallis and Landry 2001; Gerbec et al. 2005; Panda et al. 2006). Their main advantage over other conventional heating methods is rapid and uniform heating of the reaction mixture. Despite these hydrothermal strategies, the direct synthesis of metal oxide nanostructures with designed chemical components and controlled morphologies is still considerably difficult. In spite of the potential for technological applications of SnO_2 nanopowders (Jouhannaud et al. 2008; Pires et al. 2008; Wu et al. 2002), the role of heating rates and favorable conditions in the MAH method for the synthesis of SnO_2 powders was not fully reported in the literature. Our group has been able to synthesized, by means of MAH method, different crystalline, micro-, and/or nanoscale materials.(Moreira et al. 2011; Volanti et al. 2011; Macario et al. 2010).

Understanding the structural, physical, and chemical properties of SnO_2 and the changes that can be induced in its structure and consequently its other properties can offer new routes to address the challenges associated with this material. In this study, we report a direct process to obtain nanostructured SnO_2 powders through the MAH method, using low temperatures and short annealing times in an environmental synthesis. The powders were investigated and characterized by different techniques which were used as tools to investigate the structural order–disorder degree of crystalline SnO_2 samples. A friendly model to establish the relationship between quantum confinement model and order–disorder features are used to describe the optical property of tin oxide. The remainder of this article is organized as follows: the next two sections address the experimental procedures and characterization techniques. In the next section, the results are presented and discussed in detail. Finally, our main conclusions are summarized.

Experimental section

The desirable SnO_2 samples were prepared using $SnCl_4{\cdot}5H_2O$ (98\%, Aldrich) at 0.14 M as a precursor due their higher solubility if compared to $SnCl_2$. This reagent was slowly added into 200 mL of deionized water at room temperature under stirring to produce a transparent colloidal solution. In our experiments, hydrochloric acid formed after tin chloride dissolution was used as a means to dose OH− ions slowly and uniformly throughout the reaction. We found that the concentration of HCl was enhanced. Portions (100 mL) were prepared for each sample and loaded into a 110-mL sealed polytetrafluoroethene (PTFE) autoclave reaching approximately 90% of the total volume and thus providing maximum pressure efficiency to the system (Walton 2002). The product was placed in a MAH system using 2.45 GHz of microwave radiation with a maximum output power of 800 W. The reaction mixture was heated to 160 °C in 1 min (at 800 W) and was kept at that temperature for 10 (S10) and 60 (S60) min without stirring under a constant pressure of 5 bar. After the reaction, the autoclave was naturally cooled to room temperature. The solid product was washed with deionized water several times until the effluent pH was neutral and then dried at 80 °C for 12 h.

Characterizations

X-ray diffraction (XRD) powder spectra were obtained using a Rigaku DMax 2500PC instrument with Cu Kα radiation. Data were collected from 20° to 110° in 2θ range with a 0.5° divergence slit and a 0.3-mm receiving slit. Data were collected in a fixed-time mode with a 0.02° step size and a 2 s/point. The surface areas were analyzed by adsorption/desorption isotherms of N_2 employing the Brunauer–Emmett–Teller (BET) method was using Micromeritics ASAP 2000 equipment.

Thermal properties of samples were examined by TGA measurements (NEZTSCH Thermische Analyze STA409 Cell) with a heating rate of 10 °C/min up to 1,000 °C under flowing N_2 gas initially. Microstructural analyses were made by Transmission Electron Microscopy (TEM) Philips CM 200 and Field Emission Scanning Electron Microscopy (FE-SEM) Zeiss Supra™ 35. FT-Raman spectra were recorded on a RFS/100/S Bruker Fourier Transform Raman (FT-Raman) spectrometer with a Nd:YAG laser providing an excitation light at 1,064 nm having a spectral resolution of 4 cm^{-1}. UV–Visible absorption coefficients were measured with Varian Cary 5 G using an integration sphere through a total reflectance mode. PL spectra were collected with a Thermal Jarrel-Ash Monospec 27 monochromator and a

Hamamatsu R446 photomultiplier. The 350.7 nm exciting wavelength of a krypton ion laser (Coherent Innova) with the nominal output power maintained at 200 mW. All characterizations were recorded at room temperature.

Results and discussion

An analysis of the XRD results shown in Fig. 1 confirms that the S10 and S60 present cassiterite phase identified by a JCPDS card (No. 41-1445) with lattice parameters $a = b = 0.475$ nm and $c = 0.319$ nm presenting $c/a = 0.67$ in a tetragonal structure with a $P4_2/mnm$ space group. The unit cell of the rutile-type SnO_2 compound is inserted in Fig. 1. The relatively broader peaks observed from XRD patterns indicate the nanosized nature of the tin oxide which is confirmed by the HR-TEM image in Fig. 3a and the high BET surface area of 199 m^2/g. Furthermore, the S60 sample shows more intense and defined peaks, indicating a high-ordered sample. Crystallite sizes belonging to different directions are calculated from XRD data using Scherrer's theorem as given below (Cullity and Stock 2001).

$$t_{XRD} = \frac{0.9\lambda}{\beta \cos\theta} \quad (1)$$

where λ is the wavelength of the incident X-rays (0.15406 nm), β is full-width at half maximum (FWHM), and θ the diffraction angle. Crystallite sizes are listed in Table 1 suggest small changes in absorbance/emission phenomena due to the slight increase on crystallite sizes of S60 sample.

Thermogravimetric analysis and synthesis procedures

Figure 2 reports the results of the thermogravimetric analysis of S60 performed over temperatures from 20 to 1,000 °C in N_2 atmosphere. For sample S60, the nanoparticles show a total weight loss around 11% between 20 and 1,000 °C. The largest rate of weight loss, 6%, is detected from 20 to 150 °C, possibly due to the loss of the residual water remaining in the as-dried powder. This fact can be associated with

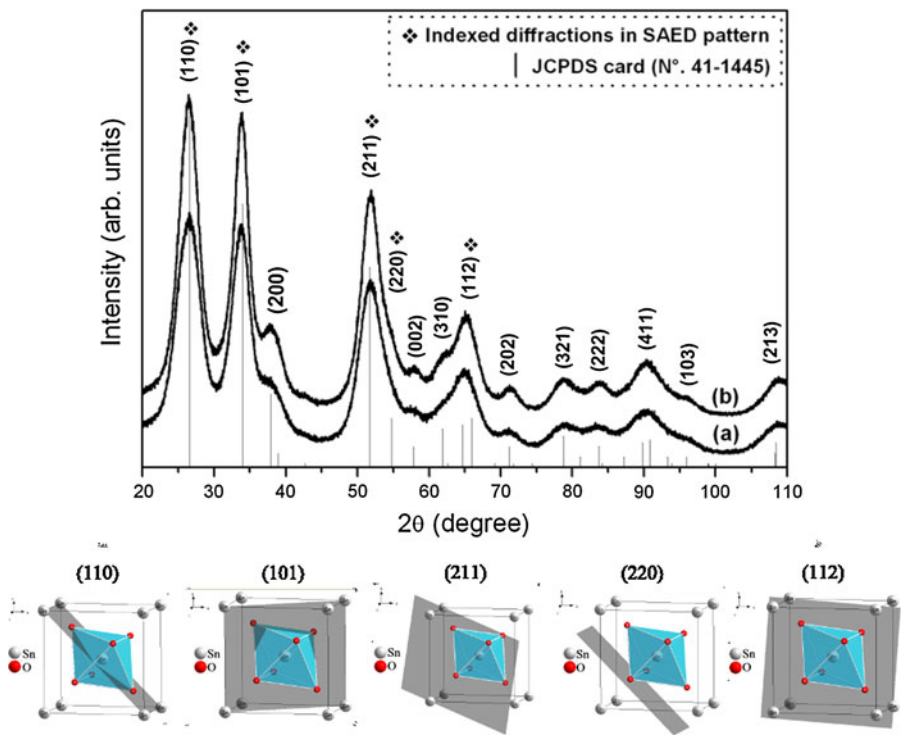

Fig. 1 X-ray patterns of SnO_2 typical nanosized powders annealed at 160 °C for (*a*) 10 (S10) and (*b*) 60 (S60) min using a hydrothermal microwave method

Table 1 Crystallite sizes of tin oxide at different directions

Sample	(110)	(101)	(211)	(112)	Average size
S10 (nm)	2.6	3.6	2.9	3.5	3.1
S60 (nm)	3.2	4.4	3.2	4.2	3.7

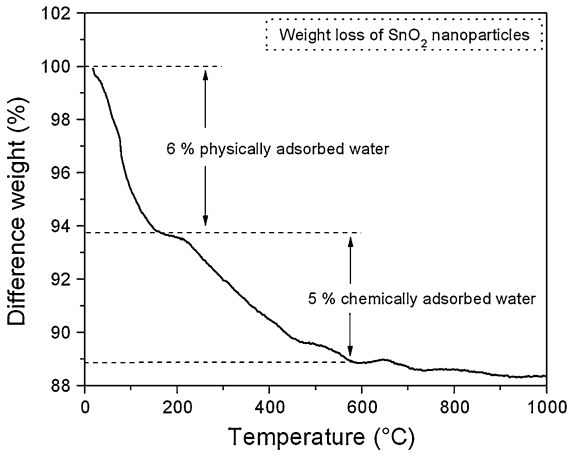

Fig. 2 TGA of SnO_2 nanosized particles annealed at 160 °C for 60 (S60) min using a hydrothermal microwave

desorption of physically adsorbed water on the surface of the particles. For an unmodified SnO_2 powder, a second weight loss ($\approx$5%) can be attributed to continuous dehydroxylation of the particle surface and boundaries which occurs continuously between 160 and 550 °C. The corresponding values (Majdoub et al. 1996) are commonly expected for samples prepared by hydrothermal methods.

Favorable conditions for the formation of SnO_2 nanoparticles are supported by hydrolysis of stannic chloride precursor, forming the stannic acid followed by the reaction of $Sn(OH)_4$ formation and dehydration, which through dehydration process became able to form SnO_2 rutile type nanocrystals as described by reactions 2 and 3. Other important element is water viscosity, which under hydrothermal conditions may be reduced with temperature increases. Even under milder conditions, the viscosity is still lowered (Rabenau 1985), and thus it is possible that the mobility of dissolved ions and molecules is higher under hydrothermal conditions than at ambient pressures and temperatures. Therefore, electromagnetic microwave radiation acts directly on the permanent dipole of the water (rotational barriers) employing uniform ratings (Wilson et al. 2006). This phenomenon is dependent on the capability of a specific compound (solvent or reagent) to absorb microwave radiation and convert it into heating (Kappe 2004; Huang and Richert 2008). Due to the difference in the solvent and reactant dielectric constants, selective dielectric heating can provide significant enhancement in the energy transfer process directly to the reactants, which causes an instantaneous internal temperature rise. Using metal precursors that have large microwave absorption cross sections relative to the solvent, very high effective reaction temperatures can be achieved. Therefore, this fact allows the rapid decomposition of the precursors, thus creating highly supersaturated solutions where nucleation and growth can take place to produce the desired nanocrystalline material.

$$SnCl_4(s) + 8H_2O(l) \rightarrow Sn(OH)_4(s) + 4Cl^-(l) + 4H_3O^+(l) \quad (2)$$

$$Sn(OH)_4(s) \rightarrow SnO_2(s) + 2H_2O(l) \quad (3)$$

These factors also enhance the magnitude of the crystallization kinetics behavior (Rao et al. 1999; Komarneni et al. 1992) due to the increase of effective collision rates among the dissolved ions and molecules in the solution. Effective collision rates occur when particles collide, producing irreversibly oriented attachments. If these particles are already crystalline, then the action of the microwave radiation on the physically and chemically adsorbed water by the particles can happen throughout the growth of the crystals. However, even in the S60 samples significant changes in particle sizes were not found, and thus the particle growth rate remains low although the SnO_2 nanosized crystallization is favored. This effect is also promoted by the high nucleation rate as a result of a fast heating rate (160 °C over 1 min) and a low growth process attributable to the short times employed.

After the nucleation process, the nanoparticles are immersed in a liquid that begins to present a certain resistance to their mobility. This behavior can be associated with the fact that nucleated nanoparticles are larger than dissolved ions in the solution. This particular environment seems to contribute to the low crystal growth process. Another aspect that can be used to control the growth process of the nanoparticles is the reduced concentration of the solution which reduces the volumetric concentration and keeps the collision rate low.

Table 2 summarizes the most reported methodologies employed in the synthesis of pure cassiterite SnO_2 which require elaborate routes followed by higher temperatures and longer times making these methods more expensive and difficult than the MAH method. All these methodologies are useful and efficient, the comparison is important to emphasize the efficiency of our methodology.

Electron microscopy

The S60 sample displayed in Fig. 3 presents low dispersed nanoparticle distributions with diameters around 3 until 5 nm as it is displayed in the HR-TEM image of Fig. 3b, c. Crystallite sizes obtained from XRD analysis belong to the same size range available from microscopies, so it is possible to assign each SnO_2-MAH nanoparticles as a crystalline single domain.

An analysis of the SEM results yields that small particles are agglomerated with a higher-sized structure. The small particles have a nearly spherical shape and they can be arranged in different ways. The selected area electron diffraction (SAED) pattern in Fig. 3a shows concentric rings that can be indexed as {110}/{101}, {211}, {220}, and {112} cassiterite SnO_2 phase in agreement of XRD patterns. Diffraction peaks related to both Sn or SnO are not sensed, indicating that the nanospheres are mainly SnO_2. The homogenous intensity of the ring can be considered as a probe to determine that the aggregates present a polycrystalline nature as it is confirmed by a HR-TEM image. The distance of 3.3 Å shown in Fig. 3a, c is related to (110) planes of SnO_2. Furthermore, the high TEM image (Fig. 3a, c) reveals their spherical-like morphology which remains unchanged for all annealing times. The aggregation process, as it is observed in Fig. 3d, can be associated with the adhesion among the nanoparticles which reduces their

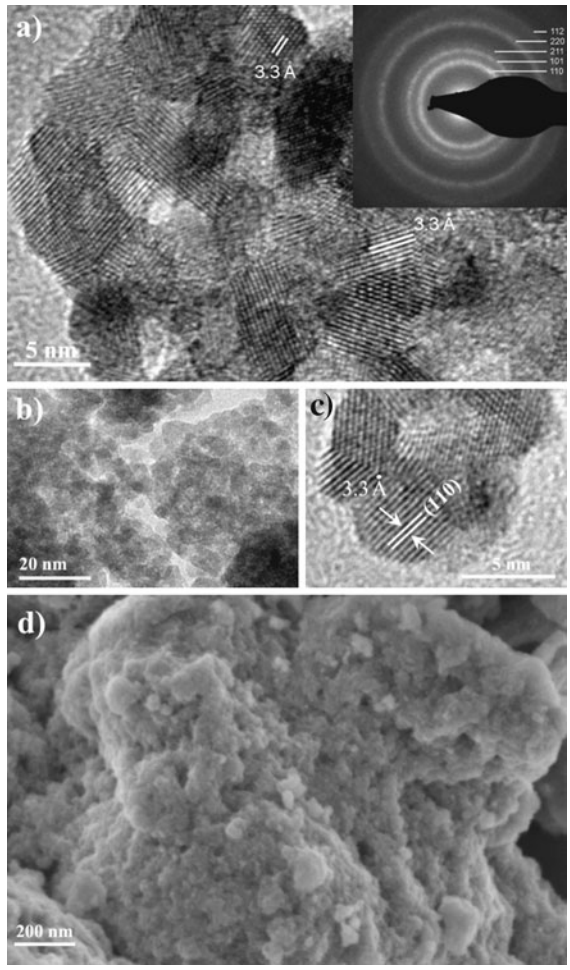

Fig. 3 **a**, **b** TEM image, **c** high-TEM of spherical-like particles, and **d** FE-SEM image of SnO_2 nanoparticles

Table 2 Comparative evaluation among different methods for obtaining of SnO_2 nanosized ceramics

Method	*T* (°C)	*t* (min)	Size (nm)	References
SSR	600	120	12.5	Chen et al. (2003)
SG	450	15	300	Dal Santos et al. (2003)
CS	150	3,000	4	Lee et al. (2006)
Solvothermal	180	1,440	3.5	Liu et al. (2008)
MAIL	160	10	2,500	Dong et al. (2008)
MAH	180	120	5	Jouhannaud et al. (2008)
MAH	100	240	5.5	Krishna and Komarneni (2009)
MAH	160	10	3–5	This study

SSR solid state reaction, *SG* sol–gel, *CS* colloidal suspension, *MAIL* microwave-assisted ionic liquid, *MAH* microwave-assisted hydrothermal

surface energy because primary particles have tendency to form small aggregations. By forming a nearly spherical or equi-axed arrangement, a minimum surface free energy can be achieved (Gervais and Kress 1985).

Raman spectroscopy

Raman selection rules for rutile-type SnO_2 nanoparticles belong to the point group D_{14}^{4h}, space group $P4_2$, and $Z = 2$ in the tetragonal structure (Zhou et al. 2006a) which can be observed in Fig. 4. The normal lattice vibration at Γ points of the Brillouin zone of this system are given on the basis of group theory:

$$\Gamma = A_{1g}(R) + A_{2g} + B_{1g}(R) + B_{2g}(R) + E_g(R) + 2^a_{2u}(IR) + 2B_{1u} + 4E_u(IR).$$

where R indicates Raman active bands and IR indicates infrared active bands (Katiyar et al. 1971). Among them, A_{1g} at 631 cm^{-1}, E_g at 479 cm^{-1}, and B_{2g} 776 cm^{-1} represent three first-order Raman active modes of rutile SnO_2 powders. In Raman active modes, the oxygen atoms vibrate, while the Sn atoms remain practically motionless. Modes A_{1g} and B_{2g} vibrate in the plane perpendicular to the *c*-axis, while the E_g mode vibrates in the direction of the *c*-axis (Abello et al. 1998). In addition to the fundamental Raman peaks of rutile SnO_2, another wide absorption band is observed at 560, 426, and 354 cm^{-1} corresponding to B_{1u}, A_{2g}, and E_u modes, respectively, which is commonly inactive for Raman measurements (Dieguez et al. 2001; Scott 1970).

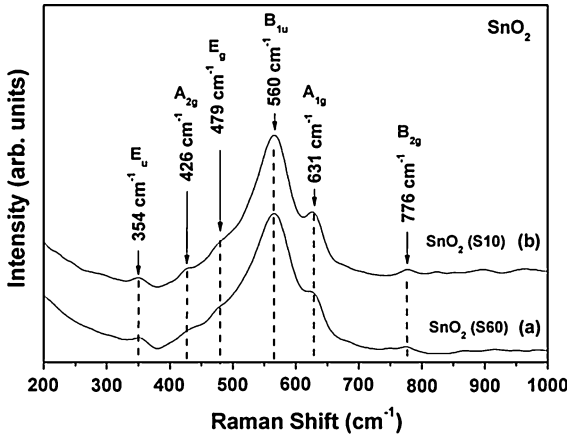

Fig. 4 Raman spectroscopy of SnO_2 nanoparticles synthesized for (*a*) 10 min (S10) and (*b*) 60 min (S60)

Some inactive modes in bulk material can be active for small particles or nanostructures due to the size effects, and it is plausible to take into account that the inactive mode becomes active with decreasing particle sizes (Trayler et al. 1971; Shek et al. 1999). The broad peak at 354 cm^{-1} was also reported in extra-fine (3–5 nm) nanoparticles (Yu et al. 1997; Kuiri et al. 2007) while it was not observed in the microcrystalline SnO_2 powders, which is in accordance with XRD and HR-TEM results. This phenomenon can be attributed to the relaxation of the Raman selection rule by the reduction of the particle size to few nanometers as well as by the high concentration of defects in surface sites such as oxygen vacancies and lattice disorders (Scott 1970) provoked by the forced hydrolysis of $SnCl_4$ solutions (Fig. 2). On the other hand, following the work of Scott (1970), we can propose that for SnO_2 nanopowders, the vibrational modes around these regions arise either as a consequence of a reduction in the particle dimension or are related to the conversion from the amorphous-to-crystalline phase (Scott 1970). However, in the present case, the XRDs have been identified as crystalline tin oxide even for S10 and S60 samples. Thus, the appearance of a quite intense peak near 560 cm^{-1} cannot be related to the amorphous phase. The appearance of this peak might be considered as a consequence of the reduced particle size (Table 2) and defects in the surface as well as the interface between the particles (Li et al. 2007; Longo et al. 2008). Furthermore, as observed in Fig. 4, all typically Raman active modes (together the non-typically active modes) are better defined in sample S60 than in sample S10, indicating that the S10 sample has a different order degree.

Photoluminescence and UV spectroscopies

It is well known that PL emissions are dependent among other factors, by the structure and the presence of defects or impurities of the material. In 1980, Blattner et al. have been reported that in pure SnO_2 single crystal the PL emissions present three peaks at 3.37 eV (366 nm), 3.28 eV (376 nm), and broad peak at 2.5 eV (494 nm), associated to acceptor level, donor–acceptor pairs, and oxygen vacancies concentration, respectively, while for low-dimensional SnO_2 nanostructures a PL peak centered at 2.09 eV (591 nm) has been observed. The PL of bulk SnO_2 is

generally attributed to defect levels within the band gap, associated with oxygen vacancies or Sn interstitials in the crystalline structure (Pan et al. 2008); however, its origin in nanostructured SnO_2 is far from being clearly established due to the variety of structures, which yield various PL emission patterns. Recently, our efforts have been focused to elucidate two different origins of PL emissions found to S10 and S60 samples present in Fig. 5 (Longo et al. 2009). Strong and weak defects generate shallow and deep intermediate states inside the band gap as schematically represented in the inset of Fig. 5 and estimated using UV–Vis measurements from Fig. 6. Using hυ (3.52 eV) as excitation source, the populated states are able to recombine through a photon emission related to specific populated states generated from the perturbation on the density of states. The violet–blue emission around 438 nm (high energy) can be attributed to recombination among shallow defects inside the band gap (see the inset in Fig. 5) while the orange–infrared emission around 764 nm are linked to deep states (low energetic defects) inserted in the band gap and this effect are capable to produce a disorder in the periodic lattice (Longo et al. 2009). Çetin and Zunger (2002) and Trani et al. (2008) have calculated the band structure of SnO_2 and predicted that the energy level of the oxygen vacancy with two electrons is shallow within the band gap, which acts as the n-type donors.

It is well known that the band gap of SnO_2 nanostructures exhibits a pronounced blue shift as comparable to those of the bulk counterparts (Zhu et al. 2010). Through first-principles calculations, Deng et al. (2010) reported the band gap of SnO_2 nanostructures increases with decreasing the effective diameter as can be seen in Table 1. Generally speaking, these results are related to the quantum confinement. In fact, as it has been remarked by Sun et al. (2003) the electronic properties of nanostructures are effectively tuned by the presence broken bonds and nonbonding electrons at the nanoscale (Sun 2010). Thus, these uncoordinated atoms generating an excess of energy associated with surface atoms that will significantly influence on the band structure of nanostructures forming energy states in the mid-gap region. In this respect, very recently, Zhu et al. (2010) have

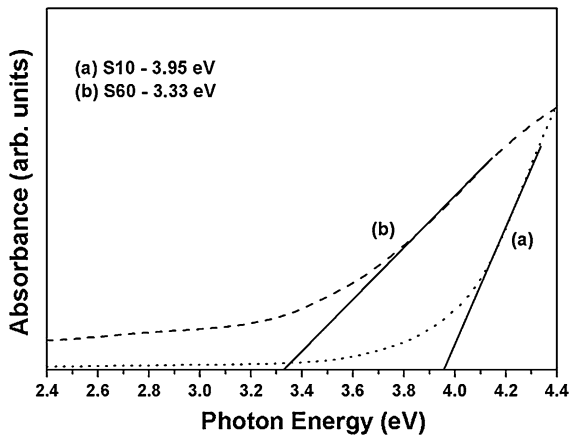

Fig. 6 UV–Vis absorbencies for S10 (*a*) and S60 (*b*) samples using the reflectance mode in an integration sphere

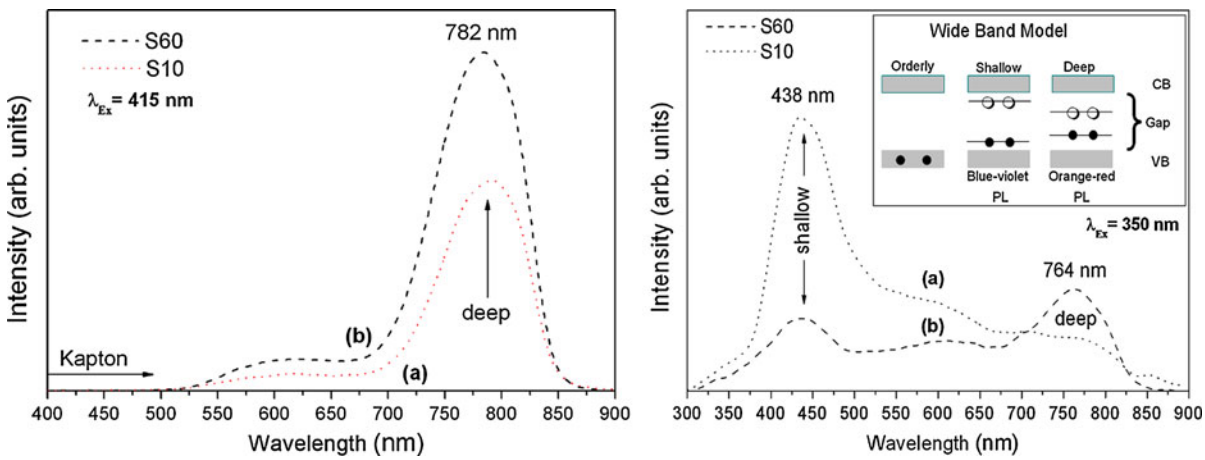

Fig. 5 Photoluminescence of SnO_2 nanoparticles synthesized for (*a*) 10 min (S10) and (*b*) 60 min (S60) under 415 and 350 nm of exciting wavelengths

established an analytical model to address the band gap shift in SnO_2 nanostructures in self-equilibrium state on the basis of bond length and bond energy correlations and this band gap shift is attributed to the lattice strain and coordination imperfection in the surfaces of SnO_2 nanostructures.

The wide band model (Pontes et al. 2003) (see the inset in Fig. 5) shows the most important events occurring along the excitation. The emission profile occurs by several paths involving numerous states within the forbidden band gap (Moreira et al. 2009) via a multiphonon process through shallow and deep states generated by different types of defects related to the synthesis methods employed.

PL results indicate the existence of two specific emission centers promoted by shallow (high energy) and deep (low energy) defects, respectively. These defects were not significantly influenced by the decreasing in the excitation energy, i.e., if the wavelength is changed from 350 to 415 nm. In the excitation of 415 nm the fist PL peak was completely quenched due to the use of *Kapton* filter, which is necessary because this is appropriated to cut the excitation line (415 nm). Thus, the high-energy defects are suppressed and orange emission is enhanced, favored by low-energy excitation. Under high-energy excitation (350 nm) the shallow defects appear to be suppressed with synthesis time increases from 10 to 60 min. The fraction of defects related with surface states and random oxygen vacancies decreases significantly while defects related to structural distortions become more evident. In this context, it is important to cite the very recent study of Zhou (2010) in which reversed crystal growth process can be operative in our case. From this study, the PL behavior can be explained due to crystallization extends from surface to the core, and, therefore the surface defects decreases as the synthetic time increases. In addition, a somewhat similar behavior has been also observed by Gaidi et al. (2010) for ultrathin films of SnO_2 nanoparticles synthesized by means of pulsed laser deposition. These authors shows that surface state, e.g., oxygen vacancies dominate completely the PL emission of SnO_2 nanoparticles, which becomes more luminescent as the nanoparticles size decreases while the PL energy remains unchanged. For S10 samples, the $\rho(s)$ (shallow defects density) is larger than $\rho(d)$ (deep defects density), while for S60 an opposite behavior is evident. This remark may be supported by XRD and Raman features. The PL band is red-shifted while the crystallite D value increases and ultimately favors an increase in the visible orange emission. A similar trend of the band shift with D values has been reported in ZnO nanocrystals and is attributed to a quantum size effect like a quantum confinement (Kim and Fujita 2002).

These results are confirmed by an analysis of the results of UV–Vis optical absorbance presented in Fig. 6. The decreases of defect $\rho(s)$ yield a reduction of states within the band gap for the S60 sample. On the other hand, the improved crystallization and consequently the whole redistribution on the density of states, leads the band gap value more closely to SnO_2 bulk samples as can be seen follow. The optical band gap (E_g) of nanocrystals was estimated using the classical Wood and Tauc equation. For instance, the extrapolated linear portion of the curve in Fig. 6 (the straight lines to the x axis) of E_{photon} at $\alpha = 0$; Eq. 4 gives absorption edge energies corresponding to $E_g = 3.95$ and 3.33 eV for the S10 and S60 samples, respectively. α is obtained directly from the Munk–Kubelka equation.

$$(\alpha h\upsilon) = A\left(h\upsilon - E_g\right)^n \tag{4}$$

where υ is the frequency, A is a constant, and n can assume different values depending upon the mode of interband transition as follows: 1/2 for direct allowed, 3/2 direct forbidden, 2 for indirect allowed, and 3 for indirect forbidden. Radiative recombination between shallow and deep trapped electrons and trapped holes in tail and gap states are mainly responsible for PL emission (Leite et al. 2003; Chen et al. 2003; Zhou et al. 2006b). The absence of an intense emission related to direct recombination from the conduction band (CB) to the valence band (VB) as a free exciton decay indicates that part of the excitation energy (3.52 eV) is lost by electron phonon interaction. Although, slight contributions of this band-to-band transition (347 nm) comprise the violet–blue emission region mainly for S60 sample, as a slight shoulder at this region. These results point out that the hydrothermal method assisted by microwave radiation can be considered as a synthetic procedure to obtain a highly ordered cassiterite phase at short times and discharge heating rates.

Conclusion

The main results of this study can be summarized as follows: (i) uniform nanopowders of SnO_2 (rutile-type structure) were successfully synthesized by the MAH

method at 160 °C using time ranges from 10 (S10) and 60 (S60) min. Pure cassiterite tetragonal phase was formed by previous hydrolysis of chloride precursor followed by dehydration of $Sn(OH)_4$ and finally SnO_2 nanoparticles crystallization as evidenced by a well-defined XRD pattern. Spherical-like morphology with mono-dispersed nanosized distribution around 5 nm was obtained. These results point out that MAH can be considered as a synthetic procedure to obtain a highly ordered cassiterite phase at short times and discharge heating rates. (ii) TGA data have been obtained to quantify the chemical and physically adsorbed water by the nanoparticles. These results were completed by FT-Raman spectra which showed a new broad peak around 560 cm^{-1} related to induced defective surface modes. Structural distortions in SnO_2 nanoparticles at short- and medium-range order yield a redistribution of the density of states into the material band gap. (iii) SnO_2 nanoparticles exhibit a markedly enhanced room temperature PL emission at a wavelength excitation of 350 nm can be considered as an example of the reduced defect-related behavior. Their two broad bands at 438 and 764 nm can be associated to possible confinement effects. In addition, the change of the excitation energy to 415 nm does not modify significantly the profile for the PL emission, indicating a weak dependence of excitation and emission for tin oxide nanoparticles. UV–Vis spectra shows substantial changes in the optical absorbance of crystalline SnO_2 nanoparticles while the existence of a small tail points out the presence of localized levels inside the forbidden band gap which supply the necessary conditions for the PL emission. (iv) Following the seminal works of Sun, we can propose that the structural organization at the nanoscale with the presence of uncoordinated atoms, i.e., broken bonds and nonbonding electrons, are responsible for the band gap shift in SnO_2 nanostructures, as it can be found in the corresponding PL spectra.

Acknowledgments The authors acknowledge the financial support of the Brazilian research institutions: CAPES, FAPESP, FPTI (Foundation Technological Park of ITAIPU), CNPq, and TEM facilities supplied by LMA-UNESP-Araraquara.

References

Abello L, Bochu B, Gaskov A, Koudryavtseva S, Lucazeau G, Roumyantseva M (1998) Structural characterization of nanocrystalline SnO_2 by X-ray and Raman spectroscopy. J Solid State Chem 135(1):78–85

Alivisatos AP (1996) Semiconductor clusters, nanocrystals, and quantum dots. Science 271(5251):933–937

Baruwati B, Polshettiwar V, Varma RS (2009) Glutathione promoted expeditious green synthesis of silver nanoparticles in water using microwaves. Green Chem 11(7):926–930

Batzill M (2006) Surface science studies of gas sensing materials: SnO_2. Sensors 6(10):1345–1366

Bilecka I, Niederberger M (2010) Microwave chemistry for inorganic nanomaterials synthesis. Nanoscale 2(8):1358–1374

Blattner G, Klingshirn C, Helbig R (1980) Impurity transitions in the photoluminescence spectra of SnO_2. Solid State Commun 33(3):341–344

Cai D, Su Y, Chen YQ, Jiang J, He ZY, Chen L (2005) Synthesis and photoluminescence properties of novel SnO_2 asterisk-like nanostructures. Mater Lett 59(16):1984–1988. doi:10.1016/j.matlet.2005.01.045

Cao HQ, Qiu XQ, Liang Y, Zhang L, Zhao MJ, Zhu QM (2006) Sol-gel template synthesis and photoluminescence of n- and p-type semiconductor oxide nanowires. ChemPhysChem 7(2):497–501. doi:10.1002/cphc.200500452

Çetin K, Zunger A (2002) Origins of coexistence of conductivity and transparency in SnO_2. Phys Rev Lett 88(9):095501

Chang SS, Park DK (2002) Novel Sn powder preparation by spark processing and luminescence properties. Mater Sci Eng B 95(1):55–60

Chen DL, Gao L (2004) Facile synthesis of single-crystal tin oxide nanorods with tunable dimensions via hydrothermal process. Chem Phys Lett 398(1–3):201–206. doi:10.1016/j.cplett.2004.09.055

Chen Y, Zhu J, Zhu X, Ma G, Liu Z, Min N (2003) Gas sensing property and microstructure of SnO_2 nanocrystalline prepared by solid state reaction–thermal oxidation. Mater Sci Eng B 99(1–3):52–55

Cheng B, Russell JM, Shi WS, Zhang L, Samulski ET (2004) Large-scale, solution-phase growth of single-crystalline SnO_2 nanorods. J Am Chem Soc 126(19):5972–5973

Cullity BD, Stock SR (2001) Elements of X-ray diffraction, 3rd edn. Prentice Hall, Upper Saddle River

Dai ZR, Gole JL, Stout JD, Wang ZL (2002a) Tin oxide nanowires, nanoribbons, and nanotubes. J Phys Chem B 106(6):1274–1279. doi:10.1021/jp013214r

Dai ZR, Pan ZW, Wang ZL (2002b) Growth and structure evolution of novel tin oxide diskettes. J Am Chem Soc 124(29):8673–8680. doi:10.1021/ja026262d

Dal Santos MA, Antunes AC, Ribeiro C, Borges CPF, Antunes SRM, Zara AJ, Pianaro SA (2003) Electric and morphologic properties of SnO_2 films prepared by modified sol-gel process. Mater Lett 57(28):4378–4381. doi:10.1016/s0167-577x(03)00328-8

Del Castillo J, Rodriguez VD, Yanes AC, Mendez-Ramos J, Torres ME (2005) Luminescent properties of transparent nanostructured Eu3+ doped SnO_2–SiO_2 glass–ceramics prepared by the sol–gel method. Nanotechnology 16(5):S300–S303. doi:10.1088/0957-4484/16/5/031

Deng H-X, Li S–S, Li J (2010) Quantum confinement effects and electronic properties of SnO_2 quantum wires and dots. J Phys Chem C 114(11):4841–4845. doi:10.1021/jp911035z

Dieguez A, Romano-Rodriguez A, Vila A, Morante JR (2001) The complete Raman spectrum of nanometric SnO_2 particles. J Appl Phys 90(3):1550–1557

Dong WS, Li MY, Liu CL, Lin FQ, Liu ZT (2008) Novel ionic liquid assisted synthesis of SnO_2 microspheres. J Colloid Interface Sci 319(1):115–122. doi:10.1016/j.jcis.2007.08.031

El-Sayed MA (2004) Small is different: shape-, size-, and composition-dependent properties of some colloidal semiconductor nanocrystals. Acc Chem Res 37(5):326–333. doi:10.1021/ar020204f

Epifani M, Diaz R, Arbiol J, Comini E, Sergent N, Pagnier T, Siciliano P, Taglia G, Morante JR (2006) Nanocrystalline metal oxides from the injection of metal oxide sols in coordinating solutions: Synthesis, characterization, thermal stabilization, device processing, and gas-sensing properties. Adv Funct Mater 16(11):1488–1498. doi:10.1002/adfm.200500652

Fang M, Tan XL, Cheng BC, Zhang LD (2009) SnO_2 hierarchical nanostructure and its strong narrow-band photoluminescence. J Mater Chem 19(9):1320–1324. doi:10.1039/b817530f

Gaidi M, Hajjaji A, Smirani R, Bessais B, El Khakani MA (2010) Structure and photoluminescence of ultrathin films of SnO_2 nanoparticles synthesized by means of pulsed laser deposition. J Appl Phys 108(6):063537

Gallis KW, Landry CC (2001) Rapid calcination of nanostructured silicate composites by microwave irradiation. Adv Mater 13(1):23–26. doi:10.1002/1521-4095(200101)13:1<23:aid-adma23>3.0.co;2-9

Gerbec JA, Magana D, Washington A, Strouse GF (2005) Microwave-enhanced reaction rates for nanoparticle synthesis. J Am Chem Soc 127(45):15791–15800. doi:10.1021/ja052463g

Gervais F, Kress W (1985) Lattice-dynamics of oxides with rutile structure and instabilities at the metal-semiconductor phase-Transitions of NbO_2 and VO_2. Phys Rev B 31(8):4809–4814

Gole JL, Wang ZL (2001) SnO_x nanocrystallites supported by silica nanostructures. Nano Lett 1(8):449–451. doi:10.1021/nl010048q

Her YC, Wu JY, Lin YR, Tsai SY (2006) Low-temperature growth and blue luminescence of SnO_2 nanoblades. Appl Phys Lett 89(4):3. doi:04311510.1063/1.2235925

Hu JQ, Bando Y, Golberg D (2003a) Self-catalyst growth and optical properties of novel SnO_2 fishbone-like nanoribbons. Chem Phys Lett 372(5–6):758–762. doi:10.1016/s0009-2614(03)00503-7

Hu JQ, Bando Y, Liu QL, Golberg D (2003b) Laser-ablation growth and optical properties of wide and long single-crystal SnO_2 ribbons. Adv Funct Mater 13(6):493–496. doi:10.1002/adfm.200304327

Huang W, Richert R (2008) The physics of heating by time-dependent fields: microwaves and water revisited. J Phys Chem B 112(32):9909–9913. doi:10.1021/jp8038187

Huang Y, Duan XF, Lieber CM (2005) Nanowires for integrated multicolor nanophotonics. Small 1(1):142–147. doi:10.1002/smll.200400030

Jiang LH, Sun GQ, Zhou ZH, Sun SG, Wang Q, Yan SY, Li HQ, Tian J, Guo JS, Zhou B, Xin Q (2005) Size-controllable synthesis of monodispersed SnO_2 nanoparticles and application in electrocatalysts. J Phys Chem B 109(18):8774–8778. doi:10.1021/jp050334g

Jouhannaud J, Rossignol J, Stuerga D (2008) Rapid synthesis of tin (IV) oxide nanoparticles by microwave induced thermohydrolysis. J Solid State Chem 181(6):1439–1444. doi:10.1016/j.jssc.2008.02.040

Kappe CO (2004) Controlled microwave heating in modern organic synthesis. Angew Chem Int Ed 43(46):6250–6284. doi:10.1002/anie.200400655

Katiyar RS, Dawson P, Hargreav MM, Wilkinso GRJ (1971) Dynamics of rutile structure 3. Lattice dynamics, infrared and Raman spectra of SnO_2. J Phys C 4(15):2421–2431

Kim SW, Fujita S (2002) Self-organized ZnO quantum dots on SiO_2/Si substrates by metal organic chemical vapor deposition. Appl Phys Lett 81(26):5036–5038. doi:10.1063/1.1527690

Komarneni S, Roy R, Li QH (1992) Microwave-hydrothermal synthesis of ceramic powders. Mater Res Bull 27(12):1393–1405

Krishna M, Komarneni S (2009) Conventional- vs microwave-hydrothermal synthesis of tin oxide, SnO_2 nanoparticles. Ceram Int 35(8):3375–3379. doi:10.1016/j.ceramint.2009.06.010

Kuiri PK, Lenka HP, Ghatak J, Sahu G, Joseph B, Mahapatraa DP (2007) Formation and growth of SnO_2 nanoparticles in silica glass by Sn implantation and annealing. J Appl Phys 102(2):5. doi:02431510.1063/1.2761778

Lee EJH, Ribeiro C, Longo E, Leite ER (2006) Growth kinetics of tin oxide nanocrystals in colloidal suspensions under hydrothermal conditions. Chem Phys 328(1–3):229–235. doi:10.1016/j.chemphys.2006.06.032

Leite ER, Weber IT, Longo E, Varela JA (2000) A new method to control particle size and particle size distribution of SnO_2 nanoparticles for gas sensor applications. Adv Mater 12(13):965–968

Leite ER, Paris EC, Pontes FM, Paskocimas CA, Longo E, Sensato F, Pinheiro CD, Varela JA, Pizani PS, Campos CEM, Lanciotti F (2003) The origin of photoluminescence in amorphous lead titanate. J Mater Sci 38(6):1175–1178

Li LJ, Zong FJ, Cui XD, Ma HL, Wu XH, Zhang QD, Wang YL, Yang F, Zhao JZ (2007) Structure and field emission properties of SnO_2 nanowires. Mater Lett 61(19–20):4152–4155. doi:10.1016/j.matlet.2007.01.044

Liu YK, Zheng CL, Wang WZ, Yin CR, Wang GH (2001a) Synthesis and characterization of rutile SnO_2 nanorods. Adv Mater 13(24):1883–1887

Liu YK, Zheng CL, Wang WZ, Zhan YJ, Wang GH (2001b) Production of SnO_2 nanorods by redox reaction. J Cryst Growth 233(1–2):8–12

Liu Y, Yang F, Yang X (2008) Size-controlled synthesis and characterization of quantum-size SnO_2 nanocrystallites by a solvothermal route. Colloid Surf A 312(2–3):219–225. doi:10.1016/j.colsurfa.2007.06.054

Longo VM, Cavalcante LS, Erlo R, Mastelaro VR, de Figueiredo AT, Sambrano JR, de Lazaro S, Freitas AZ, Gomes L, Vieira ND, Varela JA, Longo E (2008) Strong violet-blue light photoluminescence emission at room temperature in $SrZrO_3$: joint experimental and theoretical study. Acta Mater 56(10):2191–2202. doi:10.1016/j.actamat.2007.12.059

Longo VM, Cavalcante LS, Costa MGS, Moreira ML, de Figueiredo AT, Andres J, Varela JA, Longo E (2009) First principles calculations on the origin of violet–blue and green light photoluminescence emission in $SrZrO_3$ and $SrTiO_3$ perovskites. Theor Chem Acc 124(5–6):385–394. doi:10.1007/s00214-009-0628-7

Luo SH, Chu PK, Liu WL, Zhang M, Lin CL (2006) Origin of low-temperature photoluminescence from SnO_2 nanowires fabricated by thermal evaporation and annealed in different ambients. Appl Phys Lett 88(18):3. doi:18311210.1063/1.2201617

Macario LR, Moreira ML, Andres J, Longo E (2010) An efficient microwave-assisted hydrothermal synthesis of $BaZrO_3$ microcrystals: growth mechanism and photoluminescence emissions. CrystEngCommunity 12(11): 3612–3619

Majdoub M, Loupy A, Petit A, Roudesli S (1996) Coupling focused microwaves and solvent-free phase transfer catalysis: application to the synthesis of new furanic diethers. Tetrahedron 52(2):617–628

Mao YB, Wong SS (2005) Composition and shape control of crystalline $Ca1–xSrxTiO_3$ perovskite nanoparticles. Adv Mater 17(18):2194–2199. doi:10.1002/adma.200500437

Moreira ML, Pianaro SA, Andrade AVC, Zara AJ (2006) Crystal phase analysis of SnO_2-based varistor ceramic using the Rietveld method. Mater Charact 57(3):193–198. doi:10.1016/j.matchar.2006.01.012

Moreira ML, Andres J, Longo VM, Li MS, Varela JA, Longo E (2009) Photoluminescent behavior of $SrZrO_3/SrTiO_3$ multilayer thin films. Chem Phys Lett 473(4–6):293–298. doi:10.1016/j.cplett.2009.03.021

Moreira ML, Volanti DP, Andrés J, Montes PJR, Valerio MEG, Varela JA, Longo E (2011) Radioluminescence properties of decaoctahedral $BaZrO_3$. Scripta Mater 64(2):118–121

Orlandi MO, Ramirez AJ, Leite ER, Longo E (2008) Morphological evolution of tin oxide nanobelts after phase transition. Cryst Growth Des 8(3):1067–1072. doi:10.1021/cg7009379

Pan SS, Zhang YX, Teng XM, Li GH, Li L (2008) Optical properties of nitrogen-doped SnO_2 films: effect of the electronegativity on refractive index and band gap. J Appl Phys 103(9):093103–093104

Panda AB, Glaspell G, El-Shall MS (2006) Microwave synthesis of highly aligned ultra narrow semiconductor rods and wires. J Am Chem Soc 128(9):2790–2791. doi:10.1021/ja058148b

Paraguay-Delgado F, Antunez-Flores W, Miki-Yoshida M, Aguilar-Elguezaba A, Santiago P, Diaz R, Ascencio JA (2005) Structural analysis and growing mechanisms for long SnO_2 nanorods synthesized by spray pyrolysis. Nanotechnology 16(6):688–694. doi:10.1088/0957-4484/16/6/011

Patzke GR, Zhou Y, Kontic R, Conrad F (2010) Oxide nanomaterials: synthetic developments, mechanistic studies, and technological innovations. Angew Chem Int Ed. doi:10.1002/anie.201000235

Pianaro SA, Bueno PR, Longo E, Varela JA (1995) A new SnO_2-based varistor system. J Mater Sci Lett 14(10):692–694

Pianaro SA, Bueno PR, Olivi P, Longo E, Varela JA (1998) Electrical properties of the SnO_2-based varistor. J Mater Sci Mater Electron 9(2):159–165

Pires FI, Joanni E, Savu R, Zaghete MA, Longo E, Varela JA (2008) Microwave-assisted hydrothermal synthesis of nanocrystalline SnO powders. Mater Lett 62(2):239–242. doi:10.1016/j.matlet.2007.05.006

Pontes FM, Pinheiro CD, Longo E, Leite ER, de Lazaro SR, Magnani R, Pizani PS, Boschi TM, Lanciotti F (2003) Theoretical and experimental study on the photoluminescence in $BaTiO_3$ amorphous thin films prepared by the chemical route. J Lumines 104(3):175–185. doi:10.1016/s0022-2313(03)00014-0

Rabenau A (1985) The role of hydrothermal synthesis in preparative chemistry. Angew Chem Int Ed Engl 24(12): 1026–1040

Raghuveer MS, Agrawal S, Bishop N, Ramanath G (2006) Microwave-assisted single-step functionalization and in situ derivatization of carbon nanotubes with gold nanoparticles. Chem Mat 18(6):1390–1393. doi:10.1021/cm051911g

Rao KJ, Vaidhyanathan B, Ganguli M, Ramakrishnan PA (1999) Synthesis of inorganic solids using microwaves. Chem Mat 11(4):882–895

Ribeiro C, Lee EJH, Giraldi TR, Longo E, Varela JA, Leite ER (2004) Study of synthesis variables in the nanocrystal growth behavior of tin oxide processed by controlled hydrolysis. J Phys Chem B 108(40):15612–15617. doi:10.1021/jp0473669

Roduner E (2006) Size matters: why nanomaterials are different. Chem Soc Rev 35(7):583–592. doi:10.1039/b502142c

Scott JF (1970) Raman spectrum of SnO_2. J Chem Phys 53(2):852–853

Shek CH, Lin GM, Lai JKL (1999) Effect of oxygen deficiency on the Raman spectra and hyperfine interactions of nanometer SnO_2. Nanostruct Mater 11(7):831–835

Strauss CR, Rooney DW (2010) Accounting for clean, fast and high yielding reactions under microwave conditions. Green Chem 12(8):1340–1344

Sun CQ (2010) Dominance of broken bonds and nonbonding electrons at the nanoscale. Nanoscale 2(10):1930–1961. doi:10.1039/c0nr00245c

Sun SH, Meng GW, Wang YW, Gao T, Zhang MG, Tian YT, Peng XS, Zhang LD (2003) Large-scale synthesis of SnO_2 nanobelts. Appl Phys A 76(2):287–289. doi:10.1007/s00339-002-1506-5

Trani F, Causà M, Ninno D, Cantele G, Barone V (2008) Density functional study of oxygen vacancies at the SnO_2 surface and subsurface sites. Phys Rev B 77(24):245410

Trayler JG, Smith HG, Nicklow RM, Wilkinso MK (1971) Lattice dynamics of rutile. Phys Rev B 3(10):3457–3472

Volanti DP, Keyson D, Cavalcante LS, Simoes AZ, Joya MR, Longo E, Varela JA, Pizani PS, Souza AG (2008) Synthesis and characterization of CuO flower-nanostructure processing by a domestic hydrothermal microwave. J Alloy Compd 459(1–2):537–542. doi:10.1016/j.jallcom.2007.05.023

Volanti DP, Orlandi MO, Andres J, Longo E (2011) Efficient microwave-assisted hydrothermal synthesis of CuO sea urchin-like architectures via a mesoscale self-assembly. CrystEngCommunity 12(6):1696–1699. doi:10.1039/b922978g

Walton RI (2002) Subcritical solvothermal synthesis of condensed inorganic materials. Chem Soc Rev 31:230–238.

Wang ZL (2003) Nanobelts, nanowires, and nanodiskettes of semiconducting oxides—from materials to nanodevices. Adv Mater 15(5):432–436

Wilson GJ, Matijasevich AS, Mitchell DRG, Schulz JC, Will GD (2006) Modification of TiO2 for enhanced surface properties: finite Ostwald ripening by a microwave hydrothermal process. Langmuir 22(5):2016–2027. doi:10.1021/la052716j

Wu DS, Han CY, Wang SY, Wu NL, Rusakova IA (2002) Microwave-assisted solution synthesis of SnO nanocrystallites. Mater Lett 53(3):155–159

Yu KN, Xiong YH, Liu YL, Xiong CS (1997) Microstructural change of nano-SnO_2 grain assemblages with the annealing, temperature. Phys Rev B 55(4):2666–2671

Zhao L, Choi M, Kim HS, Hong SH (2007) The effect of multiwalled carbon nanotube doping on the CO gas sensitivity of SnO_2-based nanomaterials. Nanotechnology 18(44):5. doi:44550110.1088/0957-4484/18/44/445501

Zhou WZ (2010) Reversed crystal growth: implications for crystal engineering. Adv Mater 22(28):3086–3092. doi:10.1002/adma.200904320

Zhou JX, Zhang MS, Hong JM, Yin Z (2006a) Raman spectroscopic and photoluminescence study of single-crystalline SnO_2 nanowires. Solid State Commun 138(5):242–246. doi:10.1016/j.ssc.2006.03.007

Zhou XT, Heigl F, Murphy MW, Sham TK, Regier T, Coulthard I, Blyth RIR (2006b) Time-resolved x-ray excited optical luminescence from SnO_2 nanoribbons: direct evidence for the origin of the blue luminescence and the role of surface states. Appl Phys Lett 89(21):3. doi:21310910.1063/1.2387476

Zhu HL, Yang DR, Yu GX, Zhang H, Yao KH (2006) A simple hydrothermal route for synthesizing SnO_2 quantum dots. Nanotechnology 17(9):2386–2389. doi:10.1088/0957-4484/17/9/052

Zhu Z, Ouyang G, Yang G (2010) Bandgap shift in SnO_2 nanostructures induced by lattice strain and coordination imperfection. J Appl Phys 108(8):083511–083514